2019-01-15

Effect of anodic current density on the spreading of infiltrated nickel nanoparticles in nickel-yttria stabilized zirconia cermet anodes

P. Gasper, Y. Lu, S.N. Basu, S. Gopalan, U.B. Pal. 2019. "Effect of anodic current density on the spreading of infiltrated nickel nanoparticles in nickel-yttria stabilized zirconia cermet anodes" Journal of Power Sources, Volume 410, pp.196-203. https://doi.org/10.1016/j.jpowsour.2018.11.002
https://hdl.handle.net/2144/47024

P. Gasper, Y. Lu, S.N. Basu, S. Gopalan, and U.B. Pal, "Effect of anodic current density on the spreading of infiltrated nickel nanoparticles in nickel-yttria stabilized zirconia cermet anodes", *Journal of Power Sources*, **410**, 196-203 (2019), https://doi.org/10.1016/ j.jpowsour.2018.11.002

Effect of anodic current density on the spreading of infiltrated nickel nanoparticles in Ni-YSZ cermet anodes

Authors: Paul Gasper[1], Yanchen Lu[1], Soumendra Basu[1, 2], Srikanth Gopalan[1, 2], Uday Pal[1, 2, *]

Affiliations:

1. Boston University Division of Materials Science and Engineering
2. Boston University Department of Mechanical Engineering

*. Corresponding Author – Tel: (617) 353-7708, Email: upal@bu.edu

Abstract

Nickel – yttria stabilized zirconia (Ni-YSZ) anodes for solid oxide fuel cells were infiltrated with nickel nanoparticles with the objective of improving its performance by increasing the density of triple phase boundaries (TPBs). However, the nanoparticles deposited on the YSZ grains are not connected to one another, so the additional TPBs are not electrochemically active. It is postulated that at highly humid conditions (>95% H_2O) created by high current density, nickel nanoparticles near the anode-electrolyte interface will spread and percolate, becoming electrochemically active. To study this behavior, infiltrated nickel nanoparticles were exposed to low, high and extreme humidity conditions during testing. When exposed to low humidity, no performance improvement or changes to the nanoparticle morphology was observed. At high humidity, the cell showed performance improvement and when cooled they showed nanoparticle coarsening. Exposure to extreme humidity (≈100%) caused performance to degrade back towards that of an un-infiltrated cell and severe nickel nanoparticles coarsening was observed in the cooled cell. This study validates the hypothesis that exposure to controlled high local humidity conditions can lead to the right amount of spreading of the deposited nickel nanoparticles to achieve percolation, thereby activating their TPBs and improving cell performance.

Keywords: solid oxide fuel cell, infiltration, anode, contact angle, nickel nanoparticle, Ni-YSZ cermet

Highlights:

- Nickel nanoparticles improve Ni-YSZ cermet performance after spreading
- High humidity in the electrode causes infiltrated nanoparticles to spread
- Nickel spreading percolates infiltrated nanoparticles, improving performance
- Cells without nanoparticle spreading do not show improved performance

1. Introduction

Nickel – yttria stabilized zirconia (YSZ) cermets have long been the top choice for high performing and durable fuel electrodes for solid oxide fuel cells (SOFCs). In recent years, liquid infiltration of metallic and oxide materials has been developed to synthesize Ni-YSZ cermets and further improve Ni-YSZ electrode performance and durability [1, 2]. Even without introducing new materials, infiltration of nickel into a Ni-YSZ cermet or a YSZ backbone structure improves electrode performance by decreasing the feature size of the electrode and thus increasing the density of electrochemical reaction sites [3, 4]. This is because electrochemical reactions in the fuel electrode can only occur in one dimensional regions where the nickel, YSZ, and gas phases intersect. This region is referred to as the triple phase boundary (TPB). In general, smaller features introduced by infiltration increase TPB density [4]. Infiltrated nickel nanoparticles have feature sizes of about 100 nm, compared to the average feature size of Ni-YSZ cermets, which is about 1 μm. Thus, electrodes manufactured using nickel infiltrated into a YSZ backbone have TPB densities of around 10-30 μm μm^{-3}, compared to 1-10 μm μm^{-3} for Ni-YSZ cermets [4-9]. However, the manufacturing of electrodes containing only infiltrated nickel is a time consuming process that requires many liquid infiltration cycles, and has not yet been adopted commercially. Despite the promise of other electrode architectures, Ni-YSZ cermet electrodes are still the most common fuel electrode for SOFCs.

Logically, pre-reduced Ni-YSZ cermets would have larger pores and be easier to infiltrate for improving its performance. However, little work has been published investigating the effect of nickel infiltration into pre-reduced Ni-YSZ cermet electrodes, despite being the most straightforward approach for improving the catalytic activity of Ni-YSZ cermet electrodes. This is likely due to the concern of handling and processing of the slightly fragile pre-reduced Ni-YSZ cermets. In the anode pre-reduction process, the gas tight cells are heated to 800°C, the NiO in the cermet anode is reduced to nickel by employing an inert gas with 5% H2, and then the cells are cooled back to room temperature. The cells become fragile as a result of this process. Some researchers have avoided this problem by infiltrating the NiO-YSZ electrode prior to nickel reduction [10-14]. However, these studies all manufactured their own anode supported cells, presumably with enough porosity before nickel reduction to enable liquid infiltration; this approach is not easy to replicate by other groups. It is the experience of these researchers that commercially available NiO-YSZ electrodes from several manufacturers in the US and China cannot be liquid infiltrated before nickel reduction.

To the authors' knowledge, liquid infiltration of pre-reduced Ni-YSZ anode supported SOFCs has only been studied by researchers at Haldor Topsøe A/S [15, 16]. Haldor Topsøe A/S researchers have infiltrated pre-reduced Ni-YSZ electrodes with $Ce_{0.8}Gd_{0.2}O_2$ (GDC) plus nickel and GDC plus copper. Each of these studies tested cells at temperatures between 700°C and 800°C using H_2 as fuel. Both studies demonstrate that the pre-reduction and infiltration procedure is effective at infiltrating nanoparticles into SOFC anodes. However, these studies have had dramatically different results. Kiebach et. al. [15] infiltrated GDC and nickel, but no improvement in anode performance was measured. Skafte et. al. [16] infiltrated GDC and copper, resulting in an 80% reduction of the fuel electrode area-specific resistance at 750°C in an H_2-H_2O gas mix [16]. Determining why these studies had different results is difficult, because the weight or volume percent of infiltrated GDC and nickel were not reported by Kiebach et. al. [15], and the molarity of the infiltration solution was not reported by Skafte et. al. [16], making replication difficult. Because of the lack of methodological detail, differing testing methods, and the drastic difference in results between these studies, the impact of infiltration of metallic catalysts on the performance of pre-reduced Ni-YSZ cermet anodes is still not clear.

Another issue related to infiltrating nickel into Ni-YSZ cermet electrodes is the lack of connectivity between infiltrated nickel nanoparticles. To participate in the electrochemical reaction, nickel nanoparticles must have an electrical connection with nickel of the Ni-YSZ substrate. This is an issue because liquid infiltration leads to the deposition of discrete nickel nanoparticles on YSZ [17] and they remain unconnected making their TPBs inactive. Any deposition on the nickel substrate does not contribute to additional TPB length. This can be clearly seen when examining the microstructure of the infiltrated electrode, as seen in Figure 1. The problem of infiltrated nickel connectivity can be addressed either by infiltrating enough nickel for percolation or by infiltrating an additional phase that is electronically conducting and wets the Ni-YSZ evenly. For nickel nanoparticles to percolate, the surface coverage of nickel on YSZ needs to be between 50%-60% [3, 18]. However, this approach would require repeating the infiltration procedure until about 15% of the total cell volume consists of infiltrated nickel [18]. This would consume about half of the available pore phase, which would clearly decrease gas phase diffusion and have negative consequences for overall cell performance. Haldor Topsøe A/S researches have pursued the second approach, utilizing GDC, a mixed ionic-electronic conducting oxide [15, 16]. GDC evenly deposits on both nickel and YSZ within the cermet, so it may provide an electronic pathway for the infiltrated metallic catalysts. However, the electronic conductivity of GDC is not very high, and the experimental results are not consistent, as discussed previously.

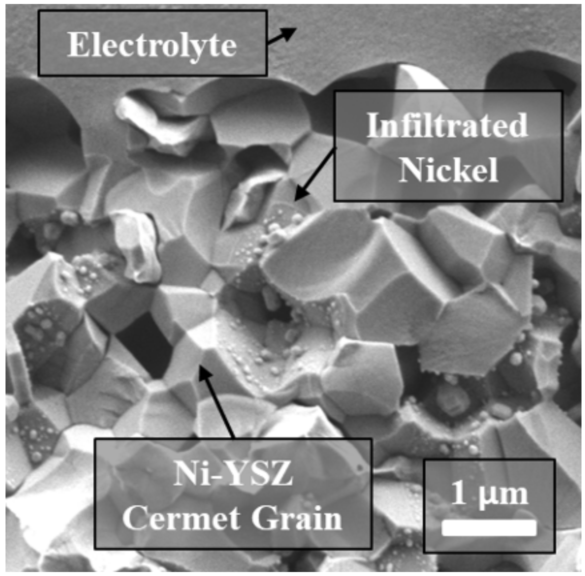

Figure 1: Anode active layer of a nickel nanoparticle infiltrated Ni-YSZ cermet after exposure to 5% H_2 – 95% Ar at 800°C.

A third possible approach for activating nickel nanoparticles is to spread the infiltrated nickel in-situ to connect them, thereby providing a percolating path for electronic conduction. This increases the surface coverage of infiltrated nickel on YSZ without requiring a large infiltrated nickel volume fraction. Nickel deposited on YSZ can be spread by exposure to high humidity. This spreading phenomena was shown experimentally by Jiao and Shikazono, who also developed a thermodynamic model to explain the variation of the Ni-YSZ contact angle as a function of the H_2 – H_2O composition in the fuel gas mix at 800°C [19]. The results of this thermodynamic model, also calculated at 750°C and 700°C, are shown in Figure 2. It is to be noted that the contact angles at different temperatures in Figure 2 are calculated for oxygen partial pressures that would not oxidize nickel as per the Ni/NiO equilibrium. The Ni-YSZ contact angle is a function of oxygen activity, which depends on the humidity in the fuel gas mix. The oxygen activity of nickel does not discernably increase until the humidity in the fuel gas mix exceeds 80%, and at 800°C the equilibrium contact angle does not fall below 90° until the humidity exceeds 95%. As the humidity increases beyond 95%, the contact angle decreases rapidly. This implies that at 800°C, the infiltrated nickel nanoparticles will spread quite rapidly when the humidity exceeds 95%. However, as the fuel gas humidity or cell temperature decreases, nickel spreading becomes much less significant. For instance, with 95% H2O – 5% H2 anodic gas mixture, the contact angle at 800°C is around 95°, and at 700°C it is about 105°; to reach a contact angle of 95° at 700°C, the anode gas humidity needs to be approximately 98%. As shown in Figure 2, this trend continues as the temperature decreases. Once the temperature is less than 700°C, nickel nanoparticles will probably not spread dramatically, even at extreme humidity values.

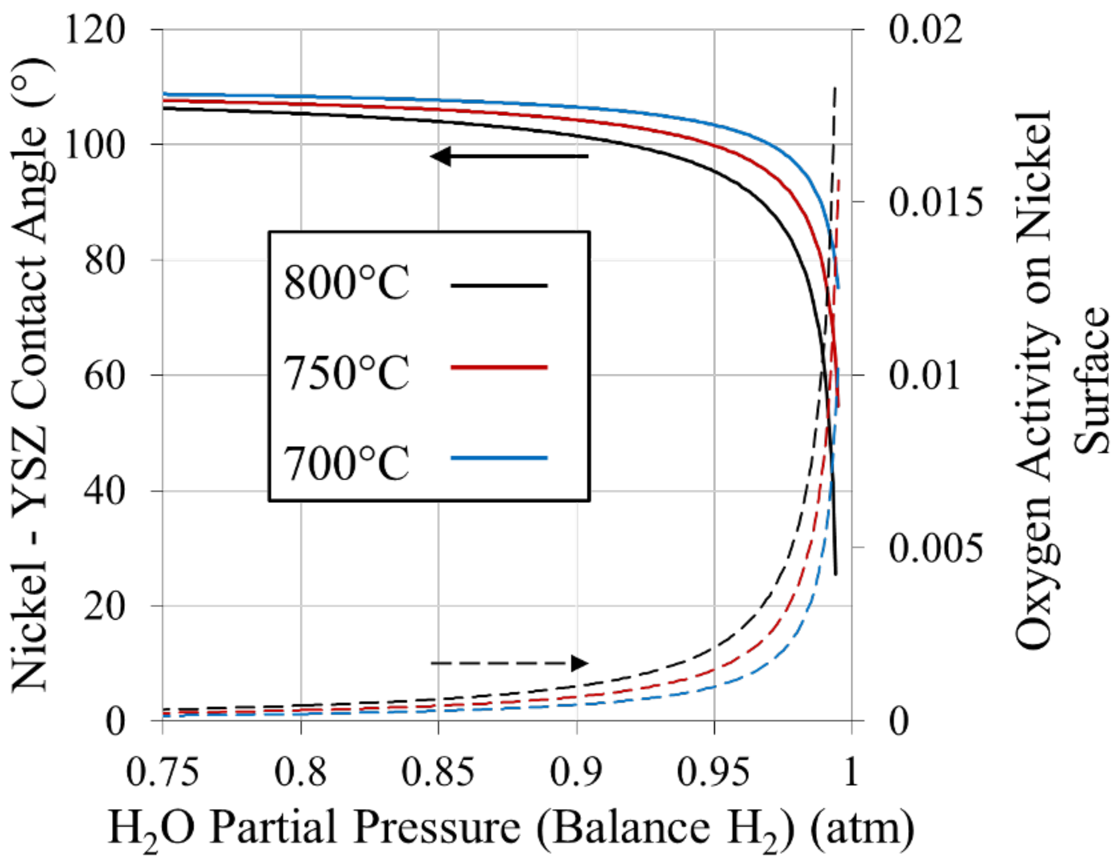

Figure 2: Contact angle between nickel and YSZ (solid lines) as a function of oxygen activity on the nickel surface. Surface oxygen activity is directly related to the humidity of the fuel gas mixture (dotted lines), shown on the secondary axis.

The current density and the humidity level in the bulk gas control the humidity at the anode-electrolyte interface. Assuming a linear concentration gradient through the anode thickness [20], the partial pressures of hydrogen and water vapor can be simply expressed for any anode by normalizing the distance through the anode thickness, x, and the current density, i. Assuming a linear concentration gradient through the anode thickness, the partial pressures of hydrogen and water vapor can be simply expressed for any anode by normalizing the distance through the anode thickness, x, and the current density, i. The distance through the anode is normalized by the total anode thickness, x_{anode}. The current density is normalized by the limiting current density, $i_{Limiting}$, which is the current density where all of the available hydrogen is consumed. Thus, the partial pressures of hydrogen and water vapor can be calculated by:

$$p_{H_2}(x,i) = p_{H_2}^{bulk}\left(1-\left(\frac{x}{x_{anode}}\right)\left(\frac{i}{i_{Limiting}}\right)\right) \tag{1}$$

$$p_{H_2O}(x,i) = p_{H_2O}^{bulk}\left(1+\left(\frac{p_{H_2}^{bulk}}{p_{H_2O}^{bulk}}\right)\left(\frac{x}{x_{anode}}\right)\left(\frac{i}{i_{Limiting}}\right)\right) \tag{2}$$

where $p_{H_2}^{bulk}$ and $p_{H_2O}^{bulk}$ are the vapor pressures of H_2 and H_2O in the bulk gas phase. The partial pressures of hydrogen and water vapor at the anode-electrolyte interface for any conditions can be calculated by setting x equal to x_{anode}. The concentration gradients of hydrogen and water vapor in Figure 3 are calculated using equations (1) and (2) assuming a 50% H_2 – 50% H_2O mix in the bulk gas for illustrative purposes, with the current density equal to $i_{Limiting}$. It is clear from Figure 3 that when the current density approaches the anodic limiting current density, a maximum of 10% of the anode's thickness is exposed to water vapor concentrations greater than 95%. This localizes nickel spreading just to the anode-electrolyte interface. At current densities less than 95% of the anodic limiting current density, the humidity at the anode-electrolyte interface is always less than 95%, and thus infiltrated nickel nanoparticles do not spread.

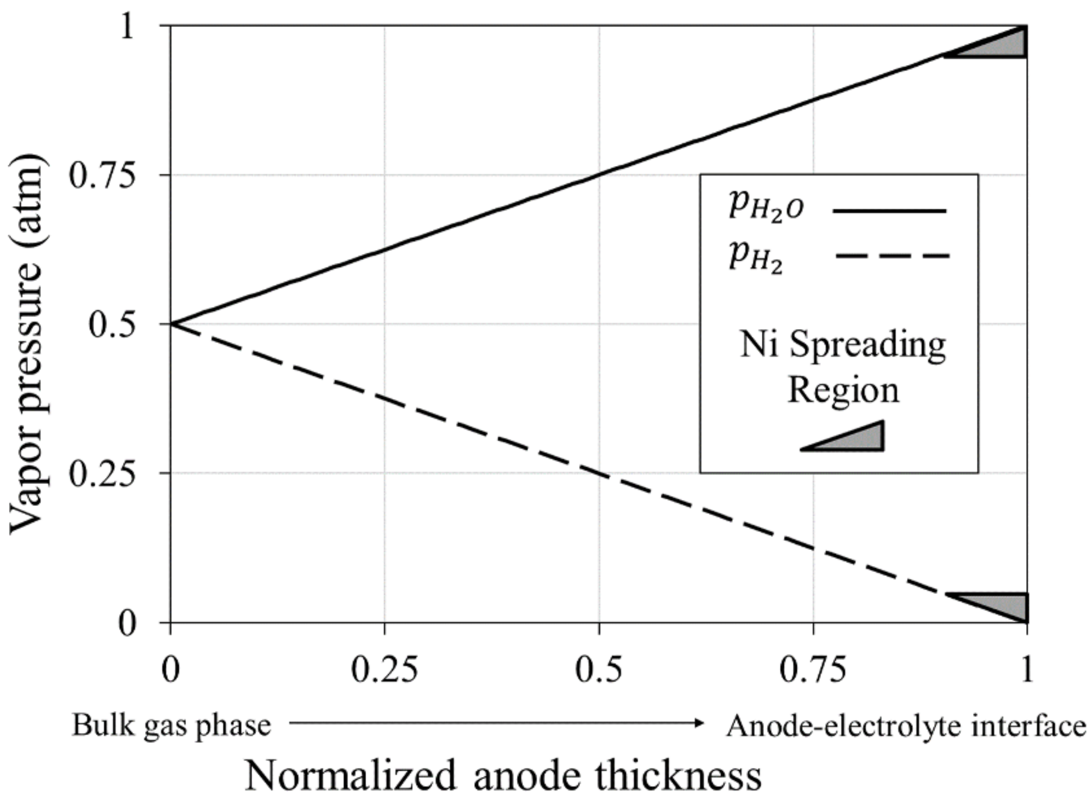

Figure 3: Concentration gradients of water vapor (solid lines) and hydrogen (dotted lines) through the anode during the application of current. The bulk gas phase composition is 50% H_2 – 50% H_2O.

During electrochemical testing, a dramatic increase in cell polarization at high current densities indicates that the anodic limiting current density has been reached. This is due to the increase of the anodic concentration polarization when almost all the hydrogen has been consumed at the anode-electrolyte interface. The anodic concentration polarization, $\eta_{conc,anodic}$, as a function of the current density i is given by:

$$\eta_{conc,anodic} = -\frac{RT}{2F}\ln\left(1-\left(\frac{i}{i_{Limiting}}\right)\right)+\frac{RT}{2F}\ln\left(1+\left(\frac{p_{H_2}^{bulk}}{p_{H_2O}^{bulk}}\right)\left(\frac{i}{i_{Limiting}}\right)\right) \quad (3)$$

where R is the ideal gas constant, F is Faraday's constant, and T is the temperature in Kelvin. Figure 3 shows the variation of the anodic concentration polarization as a function of the current density, relative to the limiting current density. In conditions with low bulk water vapor partial pressure, anodic concentration polarization increases quickly before slowing to a linear increase. This continues until the current density reaches about 90% of the limiting current density, at which point the polarization increases dramatically, thereby causing the cell potential to fall drastically. When the bulk water vapor content is high, the anodic concentration polarization is initially less and increases linearly at a slower rate until the current density reaches about 90% of the limiting current density, and then the concentration polarization again increases dramatically, causing the cell potential to fall.

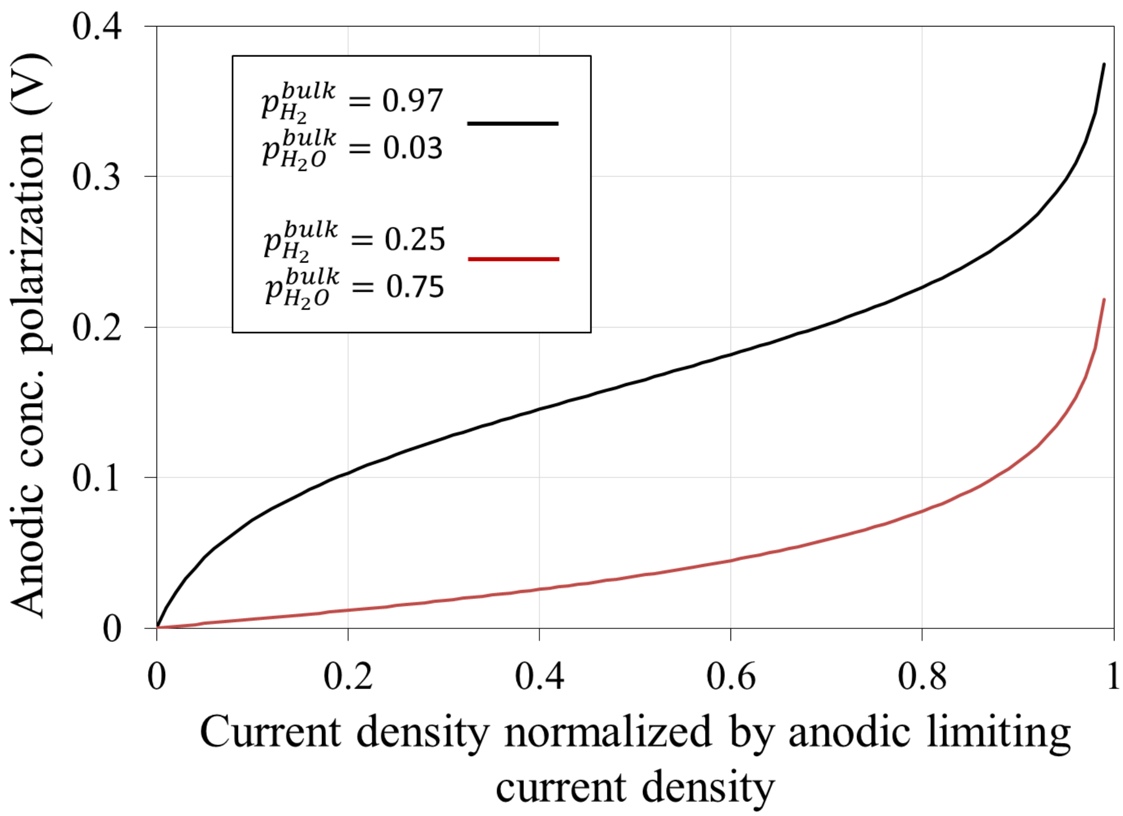

Figure 3: Anodic concentration polarization versus the current density, normalized versus the limiting current density. Two different conditions are plotted, one with low initial water vapor content (black) and one with high initial water vapor content (red).

Thus, from the previous descriptions, it is clear that the humidity at the anode-electrolyte interface, the current density, and the cell potential are all intrinsically linked. For this study, the terms high current density, high humidity at the anode-electrolyte interface, and low cell potential are all synonymous. Cells tested at high current densities have been exposed to high humidity at the anode-electrolyte interface, leading to low cell potentials; while cells maintained at low current densities have only been exposed to low humidity at the anode-electrolyte interface and maintained at high cell potentials. In this work, “high humidity” corresponds to conditions where the humidity at the anode-electrolyte interface is greater than 95%, and “low humidity” corresponds to conditions less humid. It is to be noted that the cells subjected to low and high humidity were never exposed to conditions whereby Ni oxidation took place. However, under extreme humidity conditions the cell potential is allowed to reach 0 mV, resulting in near 100% H2O vapor at the anode-electrolyte interface. This condition may lead to Ni oxidation at the anode-electrolyte interface. For this reason the exposure time to this condition was limited to within 2-3 minutes. Also, the humidity in the bulk anode vapor is not as high as that at the anode-electrolyte interface (see Figure 3) and so the Ni in the bulk anode is mostly under low humidity conditions. Hence, the overall strength and integrity of the anode structure was never compromised.

In order to test the hypothesis that nickel spreading at high humidity can activate infiltrated nickel nanoparticles, infiltrated button cells were tested at various electrochemical conditions. In the first set of experiments, infiltrated cells were tested with low humidity at the anode-electrolyte interface, by holding the current density well below the limiting current density. In the second set of experiments, which have been reported in our previous work [17], cells clearly exceeded 95% of the limiting current density, exposing them to high humidity. Lastly, an infiltrated cell was exposed to extremely high humidity by driving the cell potential to 0 V. The electrochemical behavior of these cells will provide insight into the evolution of infiltrated nickel nanoparticles during testing.

2. Methods

2.1. Cell Preparation

Anode supported SOFC buttons cells were purchased from Materials and Systems Research, Inc. Cells were composed of an 800 μm thick, 2.74 cm diameter NiO-YSZ anode supporting layer, a 12 μm thick NiO-YSZ anode active layer, and a 10 μm thick dense YSZ electrolyte. Three groups of samples were electrochemically tested, as listed in Table 1. Cathodes for group A were screen-printed onto the electrolyte, and were composed of a 15 μm thick, 1.7 cm diameter LSM-YSZ cathode active layer and a 50 μm thick LSM cathode current collector layer. Slurry for the cathode active layer was prepared by mixing LSM (Fuel Cell Materials, USA) and 8YSZ (Tosoh Corp., Japan) powders in a 1:1 wt. ratio and ball milling the mixture for 10 hours in alpha-terpineol (Alfa Aesar, USA) with pore former (Carbon lamp-black, Fisher Scientific, USA) and binder (V6, Heraeus, USA). For the cathode current collector, LSM powders were ball milled for 24 hours in alpha-terpineol with pore former and binder. After screen printing of each layer, the cathode was sintered as 1200°C for 2 hours. Cathodes for groups B and C were screen printed by MSRI with the same dimensions as above, and used as-purchased. When considering cell performance results, electrochemical measurements on cells from Group A and cells from Groups B and C are not directly compared because they have different cathodes.

Test Temperature	Group A: Low Humidity		
	Uninfiltrated Cell A	Infiltrated Cell A1	Infiltrated Cell A2

750°C	X	X	
700°C	X		X
650°C	X		X
Test Temperature	Group B: High Humidity [17]		
	Uninfiltrated Cell B	Infiltrated Cell B1	Infiltrated Cell B2
800°C	X	X	
700°C	X		X
600°C	X		X
Test Temperature	Group C: Extreme Humidity		
	Infiltrated Cell C1		
800°C	X		

Table 1: Cell nomenclature and electrochemical testing conditions

Before testing or infiltration, the as-purchased NiO-YSZ electrode was reduced to Ni-YSZ by loading the cells into a furnace between two sealed Al_2O_3 tubes and heating to 800°C at 1°C min^{-1} while flowing 1 L min^{-1} of air on the cathode side and 300 cm^3 min^{-1} of 95% Ar – 5% H_2 on the anode side for 12 hours. The apparatus was then cooled at 1°C min^{-1} to room temperature. Electrochemical performance of one cell in both group A and group B was measured after NiO reduction but without infiltration to measure the baseline performance of the uninfiltrated cell. Cells in different groups were infiltrated before electrochemical testing to measure the impact of infiltration on cell performance at different temperatures.

Cells in different groups were infiltrated before electrochemical testing to measure the impact of infiltration on cell performance under different conditions. Ni-YSZ electrodes were infiltrated using repeated cycles of vacuum infiltration of an aqueous nickel nitrate solution. The aqueous 4M $Ni(NO_3)_2$ solution was prepared by stirring 23 g nickel nitrate (Chemsavers, 99.9%), 1.8 mL Triton-X 100 surfactant (Talas) and 20 mL distilled water at 90°C. The electrode was infiltrated with the solution in a vacuum flask at 5 mbar absolute pressure. After letting the solution sit in vacuum for 30 seconds, excess solution was wiped off the electrode surface to avoid blocking pores during further rounds of infiltration. After infiltration, the cell was heated to 100°C at 2°C min^{-1} and held for 20 minutes to evaporate water, then heated to 320°C at 2°C min^{-1} and held for 20 minutes to decompose $Ni(NO_3)_2$ to NiO, then cooled to room temperature for further infiltration cycles. Five infiltration cycles were used in this study. This procedure results in the infiltration of an additional 3-4 wt% nickel, compared to the overall cell weight.

2.2. Cell Testing and Characterization

To prepare for electrochemical testing, metallic meshes were attached to the electrodes using conductive inks. Nickel ink (Fuel Cell Materials) was used to attach nickel mesh (Alfa Aesar, 99.5%) to the anode, and silver ink (Alfa Aesar) was used to attach silver mesh (Alfa Aesar, 99.9%) to the cathode. Nickel lead wires (Alfa Aesar, 99.5%) and silver lead wires (Alfa Aesar, 99.9%) were attached to the nickel and silver meshes, respectively. The cell was then loaded into the electrochemical test stand, detailed elsewhere [17]. In this test stand, the cell is placed between Al_2O_3 tubes and the anode and cathode sides are sealed using mica gaskets and glass sealing paste. For rigidity, the whole apparatus is compressed between aluminum end plates. Anode and cathode lead wires were protected by feeding them through Al_2O_3 tubes. The Al_2O_3 tubes are also used to carry the respective gas mixtures to the anode and the cathode. The cell was placed between an Al_2O_3 tube and a machined Al_2O_3 plate with mica gaskets above and below the cell. Cell temperature was measured during testing using a K-type thermocouple fed inside the cathode gas inlet tube. The cell was then compressed between the aluminum end plates using springs attached to the Al_2O_3 alignment rods. Sealing glass paste (Fuel Cell Store) was applied around the cell to ensure gas sealing.

The electrochemical test stand was then heated to 850°C at 1°C min^{-1} inside a vertical clamshell tube furnace. 300 cm^3 min^{-1} of 95% Ar – 5% H_2 was flowed on the anode side and 1 L min^{-1} of air was flowed on the cathode side during heat up. The flowrates were selected to provide the cell with excess fuel and oxidant during operation, so that fuel/oxidant depletion in the bulk gas phase is not an issue. The furnace was held for 12 hours to cure the glass paste, and then brought to 800°C at 1°C min^{-1}. Electrochemical performance was measured using a Parstat 2273A potentiostat and impedance analyzer (Ametek, Inc.) with a Kepco power booster. Before testing, an electrochemical pretesting procedure was conducted where the quality of the gas seal was ensured by monitoring cell OCV for 24 hours while flowing 300 cm^3 min^{-1} of 97% H_2 – 3% H_2O on the anode side and 1 L min^{-1} of air on the cathode side. Next performance stability was ensured by applying 0.5 A cm^{-2} current at 800°C for 24 hours or until the cell performance was constant.

After cell stability was verified, the cell temperature was changed to the desired testing temperature at 1°C min^{-1}. Performance was measured using I-V scans conducted galvanodynamically at a rate of 5 mA s^{-1}. I-V scans were conducted at several cathode oxygen contents and several anode fuel gas mixes. Cathode oxygen concentrations for testing were pure O_2 and dry air (21% O_2), during which the anode gas mixture was held at 97% H_2 – 3% H_2O. Cathode gas was dried using a desiccant before entering the furnace. The anode fuel gas mixture was varied between 97% H_2 – 3% H_2O, 75% H_2 – 25% H_2O, 50% H_2 – 50% H_2O, and 25% H_2 – 75% H_2O, during which the cathode gas mix was 21% O_2. Hydrogen was humidified using gas washing bottles filled with distilled water submerged in a heated water bath. Gas lines after the water bath were heated to 130°C to avoid condensation of water within the inlet gas tube. Water bath temperature and cell OCV were both monitored to measure gas humidity.

Testing temperatures for all cells tested are shown in Table 1. Cells from "Group A: Low Humidity" were never exposed to anodic mass transfer limited current densities during all measurements to prevent exposure to high humidity. Cells from "Group B: High Humidity" were measured until anodic mass transfer limited current density was clearly reached. The cell from "Group C: Extreme Humidity" was measured down to 0 V potential, exposing the anode active layer to almost 100% H_2O.

3. Results and Discussion

3.1. Electrochemical Performance

Before measuring performance with 21% O_2 on the cathode, a 'nickel spreading procedure' was conducted using I-V scans at 800°C with 100% O_2 on the cathode and 97% H_2 – 3% H_2O on the anode. This was done so that the contribution of cathodic diffusion to overall cell polarization could be safely neglected. Thus, as the current density increases, any dramatic decrease in cell potential is due to anodic concentration polarization. In this way, the exposure of infiltrated nickel nanoparticles to humidity before further characterization is easily controlled. During this procedure, cells from Group A never experience high humidity, as the current density is never above 1 A cm^{-2}, while cells from Group B and C were exposed to anodic mass transfer limited current densities. Cells from Group B were tested down to 400 mV at 800°C, which was clearly after the limiting current density had been reached. Infiltrated cell C1 was measured down to 0 V, exposing infiltrated nickel nanoparticles to nearly 100% H_2O. Thus, all subsequent I-V scans represent cell performance after nickel nanoparticles have been modified by exposure to different humidity levels.

After exposing cells to different ranges of current densities in pure oxygen, the cells were tested with 21% O_2 on the cathode side before lowering the furnace temperature. The electrochemical performance of the uninfiltrated and infiltrated cells from Group A is shown in Figure 4. It is immediately clear that there is no performance improvement when comparing the performance of infiltrated cells with the uninfiltrated cell. Infiltrated cell A1 showed almost identical performance compared to un-infiltrated cell A at 750°C, while infiltrated cell A2 showed slightly worse performance than the uninfiltrated cell at 700°C and 650°C. It appears that processing the cell after NiO reduction during the infiltration procedure may have adversely impacted infiltrated cell A2 and caused the observed degradation in performance.

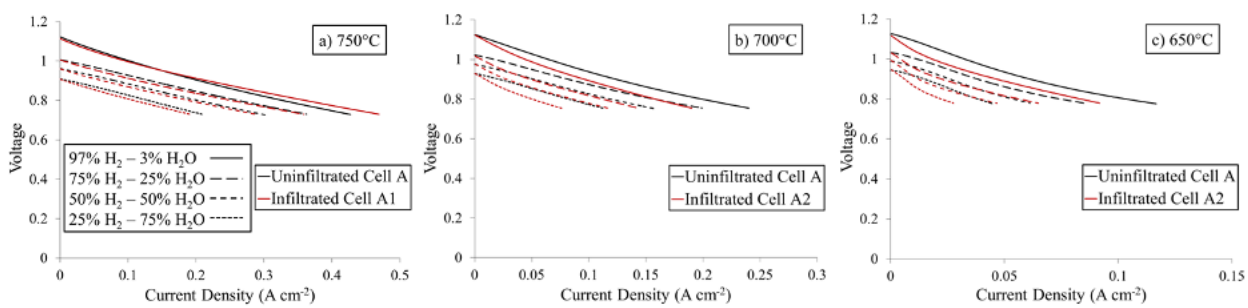

Figure 4: Electrochemical performance of Group A cells with 21% O_2 on the cathode while varying the anode gas mix humidity at a) 750°C, b) 700°C, and c) 650°C.

The electrochemical performance of the uninfiltrated and infiltrated cells from Group B is shown in Figure 5. There is a clear performance improvement at all temperatures, with the improvement increasing as temperature is reduced. Performance improvement was highest when anodic water vapor content is low, and when temperature was decreased. This is because anodic activation polarization is largest at low temperature, and to a lesser extent, at low water vapor. Thus the impact of infiltration on cell performance increases when temperature and water vapor content are decreased. More details on these results are provided elsewhere [17]. These trends imply that infiltration of nickel into the anode enhances the anodic charge transfer reaction at the anode-electrolyte interface after exposure to high humidity.

Even though cells from Group A and Group B were processed in the same manner, infiltration had a dramatic effect on the electrochemical performance for Group B but not for Group A. This suggests that the added TPBs due to the infiltrated nanoparticles had been activated during the electrochemical testing procedure for Group B cells only, specifically during the high current density exposure with pure O_2 on the cathode side, resulting in a substantial improvement in cell performance. The only difference between these two groups was the testing condition; cells from Group B were exposed to higher current densities and thus higher humidity than cells from Group A.

The electrochemical performance of infiltrated cell C1 is compared with that of uninfiltrated cell B, which was tested at the same temperature and has the same cathode (see Figure 6a). Whereas cells from group B showed significant performance improvement at 800°C, infiltrated cell C1 shows less improvement versus the uninfiltrated cell. This is evidence that exposure to extreme humidity can negate improvement due to the infiltrated nanoparticles, causing the cell performance to return back to that of an uninfiltrated cell.

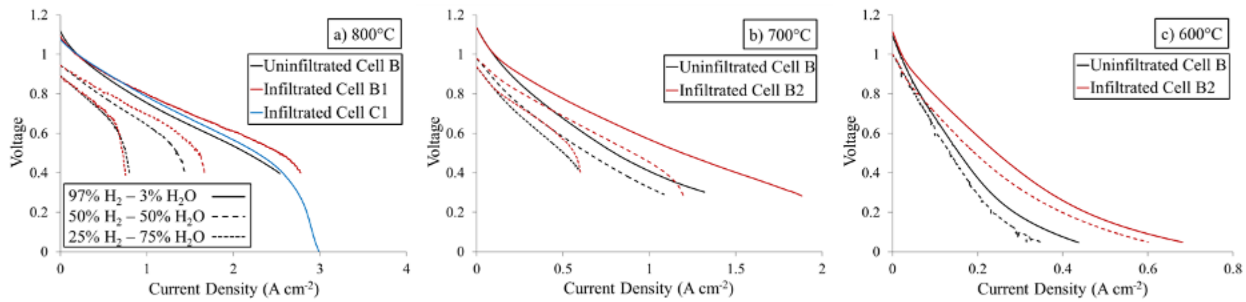

Figure 5: Electrochemical performance of Group B and C cells with 21% O_2 on the cathode while varying the anode gas mix humidity at a) 800°C, b) 700°C, and c) 600°C.

3.2. Microstructural Characterization

The microstructures of all infiltrated cells after electrochemical testing are shown in Figure 7, alongside the microstructure of an untested infiltrated cell. When qualitatively compared with each other as well as with the untested cell, it is clear that exposure to increasing humidity during testing results in the coarsening of nickel nanoparticles, when observed at room temperature. Table 2 shows the results of quantitative measurements of the nickel nanoparticles from these cells obtained by image processing of SEM fracture cross-sections, as described in more detail elsewhere [17]. The table lists the original weight gain due to nickel infiltration, the median particle size, the average particle size, and the particle density of cells in Figure 7. Nanoparticle coarsening causes both an increase in particle size as well as a decrease in particle density. Particle size can be described both by the median and the average: an increase in the median shows that the population of very small nickel nanoparticles is substantially decreased, while an increase in the average shows that particle size is larger overall. A decrease in particle density shows that nanoparticles have either coarsened together or coarsened with the nickel grains during testing.

Table 2 shows clearly that cells exposed to high humidity and high temperature experience nickel nanoparticle coarsening. Infiltrated cells B1 and C1, which were both exposed to nickel spreading conditions at 800°C, show larger particle size and lower particle density than other cells; this is evidence of nickel spreading at these conditions. For the case of infiltrated cell C1, which was exposed to extreme humidity at the anode-electrolyte interface, nanoparticle density has been dramatically reduced. Because of the dramatically reduced particle density, it was very obvious that only nanoparticles in the electrochemically active region of the anode were dramatically affected. In other regions of the anode, infiltrated nickel nanoparticles were stable. Other cells, which were maintained at lower temperatures and lower humidity, do not show strong statistical evidence of coarsening.

Since all the tested cells have similar weight gain, it is valid to compare these cells after testing. The particle statistics data provided in Table 2 for infiltrated cells A1 and A2, which have not been exposed to high humidity conditions, are quite similar and reconfirm consistency and repeatability as indicated by similar weight gains during infiltration.

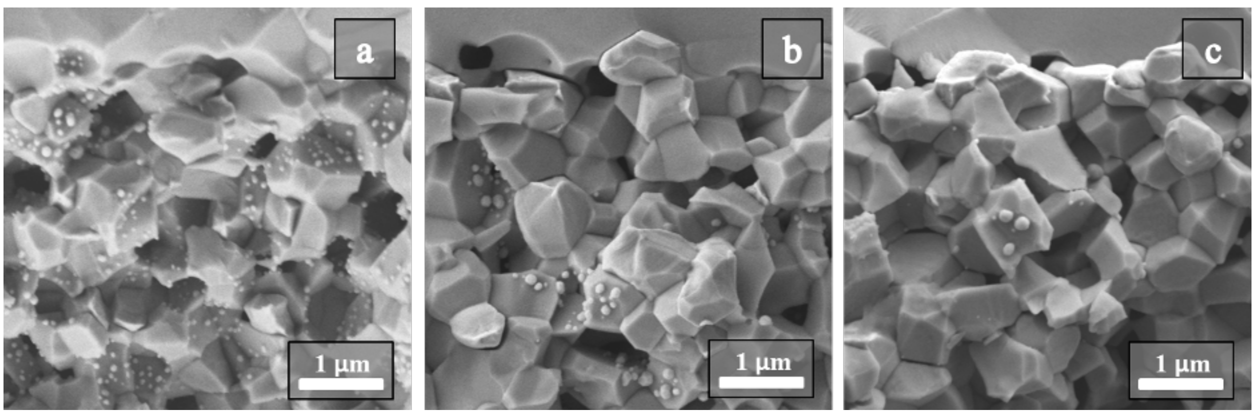

Figure 6: Fracture cross-section SEM images of the anode active layer after electrochemical testing of (a) infiltrated cell A1, (b) infiltrated cell B2, and (c) infiltrated cell C1.

Cell	Infiltration Weight Gain (wt. %)	Avg. Particle Size (nm)	Nanoparticle Density (# nm^{-2})	TPB of nanoparticles ($\mu m\ \mu m^{-3}$)
Infiltrated Cell A1	3.05	61.09	27.73	12.24
Infiltrated Cell B2	3.70	65.63	11.48	5.44
Infiltrated Cell C1	3.00	89.33	1.37	0.88

Table 2: Measured statistics of infiltrated nickel nanoparticles from analysis of fracture cross-section SEM images. Infiltrated weight gain is relative to the total weight of the cell before infiltration. Statistics were calculated from nanoparticles within a 700 μm^2 region of interest over the anode active layer.

3.3. Role of Humidity at the Anode-Electrolyte Interface on Nickel Nanoparticle Spreading and Disappearance

The spreading mechanism of infiltrated nickel nanoparticles at high temperature during electrochemical testing as a function of the current density is shown schematically in Figure 7. As deposited, nickel nanoparticles are isolated on YSZ, and thus do not contribute active TPBs. At the testing temperature and low current density (cell group A) nanoparticles do not spread significantly due to lack of exposure to high humidity. After cooling, these nanoparticles do not change appreciably. At high current densities (cell group B), infiltrated nanoparticles are exposed to humidity higher than 95% and begin to spread. This causes some nanoparticles to connect to each other and to nickel grains, activating their TPBs and improving cell performance. The performance improvement after nickel particle spreading persists even when the cell is returned back to lower current densities. The cell does not need to be constantly operated at nickel spreading conditions to realize performance improvement. However, upon cooling, percolating nanoparticles contract to higher contact angles, reducing surface coverage of the YSZ, thereby decreasing the number and increasing the diameter of particles, leading to particle coarsening. At extreme current densities and humidity (infiltrated cell C1), nickel nanoparticles wet the YSZ almost completely, with the contact angle between nickel and YSZ approaching 20°. When the surface coverage of the YSZ grains by the deposited Ni nanoparticles is very high, the active TPB density actually decreases [18]. Upon cooling, there is significant coarsening, as well as a decrease in the total volume of the Ni nanoparticles. The loss of volume can have two mechanisms: the formation of nickel hydroxide vapor phase species at extreme local humidity conditions, and the transport of nickel atoms to the larger nickel grains of the Ni-YSZ cermet. Oxidation of nanoparticles may also occur if the local humidity causes the oxygen partial pressure to exceed the Ni/NiO equilibrium value. It is unclear which mechanisms dominate.

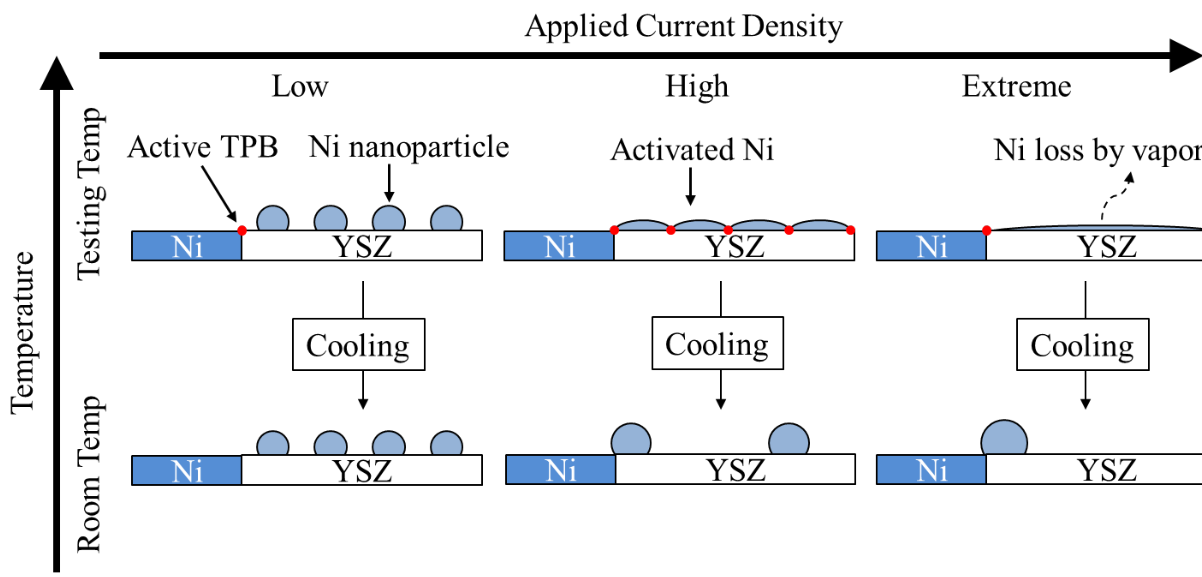

Figure 7: Schematic diagram of infiltrated nickel nanoparticle evolution during electrochemical testing and after cooling due to nickel spreading and coarsening.

4. Conclusion

Ni-YSZ cermet anodes were infiltrated with nickel nanoparticles to improve the catalytic performance of the anode. An aqueous solution of nickel nitrate was repeatedly infiltrated into the reduced Ni-YSZ electrode under vacuum and processed to produce a homogenous distribution of nickel nanoparticles. These nanoparticles were deposited on YSZ, without any obvious contact between neighboring particles. Such nanoparticles do not contribute active TPB because they are not electrically connected to one another or to the substrate. The spreading of nickel on YSZ at high humidity is proposed as a mechanism for connecting nickel nanoparticles, activating them in-situ. A thermodynamic model developed by Jiao and Shikazono [19] suggests that at humidity higher than 95%, the contact angle between nickel and YSZ drops below 90°, causing nickel to spread.

In this study, the exposure of nickel nanoparticles to humidity was controlled by testing infiltrated cells at low, high, and extreme current densities, relative to the anodic limiting current density, which is the current density where the humidity at the anode-electrolyte interface is 100%. When exposed to low current density (low humidity), the cell performance did not improve and the infiltrated nickel nanoparticles did not coarsen. At high current densities (high humidity), the cell performance did improve and the nickel nanoparticles in the anode active layer coarsened. At extreme current densities (humidity approaching 100%), the performance of the cell returns back towards that of an uninfiltrated cell while there was significant coarsening of the nanoparticles in the anode active layer.

These experimental results support the hypothesis that the spreading of nickel on YSZ causes infiltrated nickel nanoparticles to spread and percolate after exposure to high humidity, activating the nanoparticles. However, on cooling, these connected nanoparticles coarsen to larger discreet nanoparticles. Therefore, to improve cell performance and stability, nickel nanoparticles need to be exposed to sufficiently high current density to percolate the nanoparticles in the anode active region, and exposure to anodic limiting current density should be avoided.

5. Acknowledgements

This study is supported through the United States of America Department of Energy National Energy Technology Laboratory (award number DE-FE0026096). The authors would also like to acknowledge the contributions of Dr. Alexey Nikiforov, Anlee Krupp, Dr. Ruofan Wang, and Zhihao Sun.

6. References

[1] S. P. Jiang, "Nanoscale and nano-structured electrodes of solid oxide fuel cells by infiltration: Advances and challenges," *Int. J. Hydrogen Energy*, vol. 37, no. 1, pp. 449–470, 2012. DOI: 10.1016/j.ijhydene.2011.09.067

[2] Z. Liu, B. Liu, D. Ding, M. Liu, F. Chen, and C. Xia, "Review Fabrication and modification of solid oxide fuel cell anodes via wet impregnation/infiltration technique," *J. Power Sources*, vol. 237, pp. 243–259, 2013. DOI: 10.1016/j.jpowsour.2013.03.025

[3] A. Bertei, J. G. Pharoah, D. Gawel, and C. Nicolella, "Microstructural modeling and effective properties of infiltrated SOFC electrodes.," *ECS Trans.*, vol. 57, no. 1, p. 2527–2536, 10 pp., 2013. DOI: 10.1149/05701.2527ecst

[4] L. Holzer, B. Münch, B. Iwanschitz, M. Cantoni, T. Hocker, and T. Graule, "Quantitative relationships between composition, particle size, triple phase boundary length and surface area in nickel-cermet anodes for Solid Oxide Fuel Cells," *J. Power Sources*, vol. 196, no. 17, pp. 7076–7089, 2011. DOI: 10.1016/j.jpowsour.2010.08.006

[5] S. Futamura, Y. Tachikawa, J. Matsuda, S. M. Lyth, and Y. Shiratori, "Alternative Ni-Impregnated Mixed Ionic-Electronic Conducting Anode for SOFC Operation at High Fuel Utilization," *J.*

Electrochem. Soc., vol. 164, no. 10, pp. 3055–3063, 2017. DOI: 10.1149/2.0071710jes

[6] B. Hua, W. Zhang, M. Li, X. Wang, and B. Chi, “Improved microstructure and performance of Ni-based anode for intermediate temperature solid oxide fuel cells,” *J. Power Sources*, vol. 247, pp. 170–177, 2014. DOI: 10.1016/j.jpowsour.2013.08.060

[7] M. Kishimoto, H. Iwai, M. Saito, and H. Yoshida, “Quantitative evaluation of solid oxide fuel cell porous anode microstructure based on focused ion beam and scanning electron microscope technique and prediction of anode overpotentials,” *J. Power Sources*, vol. 196, no. 10, pp. 4555–4563, 2011. DOI: 10.1016/j.jpowsour.2010.12.100

[8] A. Faes, A. Hessler-Wyser, D. Presvytes, C. G. Vayenas, and J. Vanherle, “Nickel-zirconia anode degradation and triple phase boundary quantification from microstructural analysis,” *Fuel Cells*, vol. 9, no. 6, pp. 841–851, 2009. DOI: 10.1002/fuce.200800147

[9] A. Bertei, E. Ruiz-Trejo, K. Kareh, V. Yufit, X. Wang, F. Tariq, and N.P. Brandon, “The fractal nature of the three-phase boundary: A heuristic approach to the degradation of nanostructured Solid Oxide Fuel Cell anodes,” *Nano Energy*, vol. 38, pp. 526–536, 2017. DOI: 10.1016/j.nanoen.2017.06.028

[10] B. Hua, M. Li, Y. Sun, Y. Zhang, N. Yan, J. Li, T. Etsell, P. Sarkar, and J. Luo, “Grafting doped manganite into nickel anode enables efficient and durable energy conversions in biogas solid oxide fuel cells,” *Appl. Catal. B Environ.*, vol. 200, pp. 174–181, 2017. DOI: 10.1016/j.apcatb.2016.07.001

[11] M. Li, B. Hua, J. Luo, S. Jiang, J. Pu, B. Chi, and J. Li, “Enhancing Sulfur Tolerance of Ni-Based Cermet Anodes of Solid Oxide Fuel Cells by Ytterbium-Doped Barium Cerate Infiltration,” *ACS Appl. Mater. Interfaces*, vol. 8, no. 16, pp. 10293–10301, 2016. DOI: 10.1021/acsami.6b00925

[12] S. W. Kim, M. Park, H. Kim, K. Yoon, J. Son, J. Lee, B. Kim, J. Lee, and J. Hong, “In-situ nano-alloying Pd-Ni for economical control of syngas production from high-temperature thermo-electrochemical reduction of steam/CO2,” *Appl. Catal. B Environ.*, vol. 200, pp. 265–273, 2017. DOI: 10.1016/j.apcatb.2016.07.008

[13] B. Timurkutluk, C. Timurkutluk, M. D. Mat, and Y. Kaplan, “Anode-supported solid oxide fuel cells with ion conductor infiltration,” *Int. J. Energy Res.*, vol. 35, no. 12, pp. 1048–1055, Oct. 2011. DOI: 10.1002/er.1832

[14] S. Sengodan, M. Liu, T.-H. Lim, J. Shin, M. Liu, and G. Kim, "Enhancing Sulfur Tolerance of a Ni-YSZ Anode through BaZr0.1Ce0.7Y0.1Yb0.1O3- Infiltration," *J. Electrochem. Soc.*, vol. 161, no. 5, pp. F668–F673, 2014. DOI: 10.1149/2.068405jes

[15] R. Kiebach, P. Zielke, J. Høgh, K. Thydén, H. Wang, R. Barfod, and P. Hendricksen, "Infiltration of SOFC Stacks: Evaluation of the Electrochemical Performance Enhancement and the Underlying Changes in the Microstructure," *Fuel Cells*, vol. 16, no. 1, 2016. DOI: 10.1002/fuce.201500107

[16] T. L. Skafte, J. Hjelm, P. Blennow, and C. Graves, "Reactivating the Ni-YSZ electrode in solid oxide cells and stacks by infiltration," *J. Power Sources*, vol. 378, no. January, pp. 685–690, 2018. DOI: 10.1016/j.jpowsour.2018.01.021

[17] Y. Lu, P. Gasper, U. Pal, S. Gopalan, and S. N. Basu, "Improving intermediate temperature performance of nickel-yttria stabilized zirconia cermet anodes for solid oxide fuel cells by liquid infiltration of nickel nanoparticles," *J. Power Sources*, 2018. DOI: 10.1016/j.jpowsour.2018.06.027

[18] E. F. Hardjo, D. S. Monder, and K. Karan, "An Effective Property Model for Infiltrated Electrodes in Solid Oxide Fuel Cells," vol. 161, no. 1, 2014. DOI: 10.1149/2.036401jes

[19] Z. Jiao and N. Shikazono, "Study on the effects of polarization on local morphological change of nickel at active three-phase-boundary using patterned nickel-film electrode in solid oxide fuel cell anode," *Acta Mater.*, vol. 135, pp. 124–131, 2017. DOI: 10.1016/j.actamat.2017.05.051

[20] C. Bao, Z. Jiang, X. Zhang, Modeling mass transfer in solid oxide fuel cell anode: I. Comparison between Fickian, Stefan-Maxwell and dusty-gas models, J. Power Sources. 310 (2016) 32–40.